

SYSTEM IDENTIFICATION OF A TURBOJET ENGINE USING MULTI-SINE INPUTS IN GROUND TESTING

M. Many¹, M. Weber¹, S. Oberndorfer¹, S. J. Koeberle¹, B. Hosseini², M. Hornung¹

¹Institute of Aircraft Design, Technical University of Munich,

²Institute of Flight System Dynamics, Technical University of Munich
Boltzmannstraße 15, 85748 Garching, Germany

Abstract

In order to provide the transient dynamics of a miniature turbojet engine, a *JetCAT P100-RX* turbojet engine currently in use on a flying testbed is investigated. A parametric white-box model is implemented in *MATLAB/Simulink* and scaling methods for the component performance maps are applied, which are commonly used to model the compressor and turbine. Several modelling approaches of the system are investigated and compared to a phenomenological benchmark model. Subsequently, a state space representation of the considered engine is derived and the key parameters are identified using system identification techniques. A two-step approach is applied for identification: First, frequency-sweep signals are used in order to provide detailed test data over the estimated frequency span of interest. Second, optimized multi-sine input signals utilizing the initial data are injected to perform parameter identification.

Keywords

Remotely Piloted Aircraft System; RPAS; Unmanned Aerial Vehicle; UAV; Multi-Sine Inputs; State Space Representation; Turbojet Engine

1. MOTIVATION AND STATE OF THE ART

The Institute of Aircraft Design of TUM assesses new technologies in flight using custom, unmanned technology demonstrators, such as the T-FLEX demonstrator for testing of load alleviation and flutter suppression technologies in flight. As regulations prescribe the operation of unmanned aerial vehicles (UAVs) within visual line of sight, the consideration of transient dynamics of envisioned demonstrators and its subsystems during design becomes increasingly important to assure adequate performance. In this respect, the need for a more detailed model of the propulsion system in terms of achieved thrust, acceleration/deceleration capabilities and fuel consumption arises during the preliminary design phase already [1, 2]. In order to contribute to the refinement of design methods, this publication presents multiple parametric simulation models of a turbo-jet engine that are applied to model the engine *JetCat P100-RX* as a case study. The simulation model is tuned and validated using telemetry data provided by the Engine Control Unit (ECU) during ground testing.

Several attempts to model the transient behaviour of turbojet engines have been made in the past at the Technical University of Munich, [3, 4]. However, a system identification approach on such models was not attempted. In this paper, system identification is performed in the derived parametric models. One of the critical components in a physics-based model are the compressor and the turbine of the jet engine, which have a complex behaviour. In order to reliably model the behaviour of the components of the engine, the use of so-called component performance maps is common [5, 6, 7]. The component performance maps, or shortly component maps, are tailored for each engine and are usually available from the

manufacturer. However, being the product of extensive testing and experiments, they are rarely disclosed to the end user. With limited information on the component maps, like in the case of the present engine, scaling methods are a common approach to identify them from well-known or similar components, which can then be used to simulate the engine in design and off-design operating points [8]. Such a simulation is documented by Gazetta et al. [9], where a fast performing real-time simulation of nonlinear gas turbine models is studied. Furthermore, Beneda et al. applied linearization techniques on a nonlinear dynamic model of a turbojet engine to derive a linear state space representation [10, 11]. As linear systems require low computational resources, their use in design tools as well as real-time simulation and control applications is facilitated. To compensate for the inability of a linear system to describe nonlinear behaviour, multiple linear systems developed around different points of interest can be used as an alternative approach [12].

In this paper, a methodology to derive a nonlinear state space representation, which can be further used to apply system identification approaches is presented. To perform system identification tasks, the optimal control tool *FALCON.m* [13] of the Institute of Flight System Dynamics at the Technical University Munich, as well as the *MATLAB* toolbox System Identification Programs for Aircraft (*SIDPAC*) [14] are used.

2. METHODS OF TURBINE MODELLING AND PHYSICAL FOUNDATION

In this section, the working principle of the jet engine along with the governing physical equations, which are used to derive a state space representation are presented. Additionally,

a phenomenological benchmark model which is used for later performance validation, is shortly presented.

2.1. Benchmark Model for Performance Comparison

In order to evaluate the performance of the developed models, which are discussed in section 4.2, a phenomenological model introduced by L'Erario et al. is taken as benchmark model. This model is derived using the *sparse identification method for nonlinear dynamics* called SINDy [15]. In simple terms, the deduction of the model structure results from the first choice of a second order model. Subsequently, the governing terms of the model are selected from a library matrix of arbitrary candidates functions. In this model, the only required measurement for parameter identification are the thrust T and throttle input u . The derived equations are shown in Eq. 1.

$$(1) \quad \begin{aligned} \ddot{T} &= f(T, \dot{T}) + g(T, \dot{T})v(u) \\ f(T, \dot{T}) &= K_T T + K_{TT} T^2 + K_D \dot{T}^2 + K_{TD} T \dot{T} + c \\ g(T, \dot{T}) &= B_U + B_T T + B_D \dot{T} \\ v(u) &= u + B_{UU} u^2 \end{aligned}$$

with \ddot{T} the second derivative of the thrust after time, \dot{T} the first derivative of the thrust after time and u the input is here the throttle. All other symbols are parameters, which are to be identified. The choice of this model as a benchmark is justified from the fact that it appeals with its simplicity and is already proven to yield satisfying results with the *JetCat P100-RX* engine studied in this paper.

2.2. Simulation

In order to better estimate and understand the physical behaviour of the system, a white-box approach has been applied and compared to the benchmark model. The major components of the turbojet engine have been modeled using thermodynamic equations, widely documented in literature [16]. Consequently, a model of the engine has been implemented in *MATLAB/Simulink* for simulation purposes and to make use of the various system identification tools available. The dynamic model then serves as a basis for the derivation of a state space representation.

Furthermore, as the component maps are not available, the compressor and turbine performance map of the considered engine are scaled from generic performance maps using scaling factor methods and system identification techniques [6, 7]. The developed dynamic model considers the fuel mass flow rate and the atmospheric conditions as inputs, and the shaft speed, the engine Net Thrust and the Exit Gas Temperature (EGT) are observed as outputs. In the following, the derivation of the governing equations of the system is detailed. The characteristics of the engine to be modelled, according to the manufacturer, are given in TAB. 1 [17]:

Name	Value	Unit
Pressure ratio	2.9	[–]
Mass flow rate	0.23	kg s ^{−1}
Max thrust	100	N
EGT	480 – 720	°C
Exhaust Gas Velocity	1565	km h ^{−1}

TAB. 1. Nominal specifications of P100-RX engine from the manufacturer

The studied turbojet engine features a single-stage centrifugal compressor, a combustion chamber, a single-stage axial turbine and a convergent nozzle. The components of the engine are figuratively represented in FIG. 1. In order to conveniently describe the thermodynamic processes intervening in the engine, a numbering of the different stations of the engine is adopted and can also be found in Fig 1.

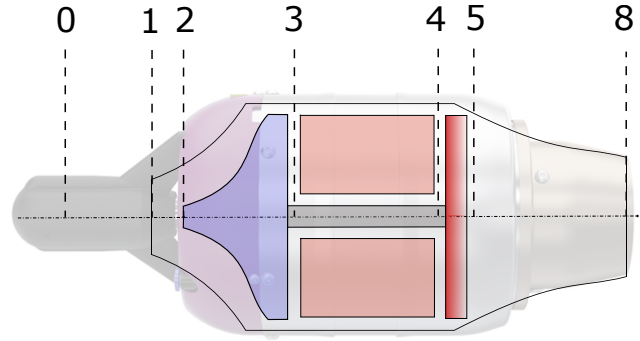


FIG. 1. Station numbering and figurative representation of the different components of the engine: inlet (1-2), centrifugal compressor (2-3), combustion chamber (3-4), turbine (4-5), nozzle (5-8)

The working principle of the engine is described in the following: The engine is started using an electric starter which rotates the shaft of the engine and enables an initial air mass flow through the system. First, the air flows through the inlet (1-2), and is then further compressed by the centrifugal compressor (2-3) to achieve a state of higher pressure and temperature. Consequently, the air is mixed with the fuel in the combustion chamber (3-4) and the resulting gas is ignited by the combustor. The hot gas, high in temperature, is subsequently expanded through the turbine (4-5), and then accelerated through the convergent nozzle (5-8).

In system identification approaches, a modelling of the system in a state space representation is common. In the scope of this work, the nonlinear state space representation in Eq. 2 is adopted:

$$(2) \quad \begin{cases} \dot{X} = f(X, U, V, \Theta) \\ Y = g(X, U, V, \Theta) \end{cases}$$

with X the state vector, U the input vector, V the vector of ambient conditions, Θ the parameter vector, Y the observation vector, f the state transition function, g the observation function. The goal of system identification for this specific

case, is to determine functions f , g and parameters Θ such that the output Y of the system matches the measurements under the same input and ambient conditions.

2.3. Governing equations

To model the system in the previously expressed state space representation, the physical processes intervening in the different components of the engine are studied and the governing equations are derived. For that, the total pressure and temperature at each station of the engine are determined. In this paper, the *stagnation* pressure and temperature and the *total* pressure and temperature, which differ by the geodetic term, are assumed to be equal, given that the size of the considered engine is small. Hence, in the following, the total pressure and temperature are calculated based on the expression of the stagnation pressure and temperature. Additionally, the gas properties of the flow before (stations 0-3) and after the combustion chamber (stations 4-8) are assumed to be constant and the subscripts a and g are respectively used to denote the quantities of interest for the air and the gas (mixture fuel/air after combustion through the combustion chamber).

Ambient variables

The vector of ambient conditions V , contains information on the ambient static pressure p_0 , the ambient static temperature T_0 and ambient air velocity V_0 . The expression of the ambient air Mach number $M_{a,0}$ is given in Eq. 3 :

$$(3) \quad M_{a,0} = \frac{V_0}{\sqrt{\kappa_a R_a T_0}}$$

with κ_a the ratio of specific heats and R_a the specific gas constant for air. From the Mach number $M_{a,0}$, the ambient total pressure $p_{t,0}$ and temperature $T_{t,0}$ can be calculated as in Eq. 4.

$$(4) \quad \begin{aligned} p_{t,0} &= p_0 \left(1 + \frac{\kappa_a - 1}{2} M_{a,0}^2 \right)^{\frac{\kappa_a}{\kappa_a - 1}} \\ T_{t,0} &= T_0 \left(1 + \frac{\kappa_a - 1}{2} M_{a,0}^2 \right) \end{aligned}$$

Inlet 1-2

The air flow through the inlet is considered fast enough to assume adiabatic flow, i.e. no exchange of energy takes place with the outside environment. Additionally, friction and aerodynamic losses through the inlet are accounted for with the assumption of a loss of total pressure. Following this, the total pressure $p_{t,2}$ and temperature $T_{t,2}$ at compressor entry can be calculated according to Eq. 5 [16].

$$(5) \quad \begin{aligned} p_{t,2} &= \text{IPR} \cdot p_{t,0} \\ T_{t,2} &= T_{t,0} \end{aligned}$$

with IPR the inlet total pressure ratio.

Compressor 2-3

The total pressure at compressor exit $p_{t,3}$ expressed in Eq. 6, can be determined by the compressor pressure ratio $\Pi_{t,C}$, which is a function of the rotational speed of the compressor and the air mass flow rate.

$$(6) \quad p_{t,3} = \Pi_{t,C} \cdot p_{t,2}$$

The total temperature at compressor exit $T_{t,3, is}$ for an isentropic flow, i.e. a perfect compression without losses, can be calculated using the isentropic relation between pressure and temperature as in Eq. 7:

$$(7) \quad T_{t,3, is} = T_{t,2} (\Pi_{t,C})^{\frac{\kappa_a - 1}{\kappa_a}}$$

In the case of the present engine, compression losses have to be accounted for and the true exit total temperature $T_{t,3}$ is expressed using the compressor isentropic efficiency η_C in Eq. 8:

$$(8) \quad \eta_C = \frac{T_{t,3, is} - T_{t,2}}{T_{t,3} - T_{t,2}}$$

Similarly to the compressor pressure ratio $\Pi_{t,C}$, the compressor efficiency η_C is also a function of the compressor rotational speed and air mass flow rate. Finally, the resulting expression for $T_{t,3}$ is given in Eq. 9:

$$(9) \quad T_{t,3} = T_{t,2} \left(1 + \frac{1}{\eta_C} \left(\Pi_{t,C}^{\frac{\kappa_a - 1}{\kappa_a}} - 1 \right) \right)$$

It can be observed in Eq. 9, that the compressor isentropic efficiency η_C and the compressor pressure ratio $\Pi_{t,C}$ govern $T_{t,3}$. Their value is usually read from component maps.

Combustion chamber 3-4

Total Pressure losses in the combustion chamber are accounted for in the combustion chamber total pressure ratio CCPR in Eq. 10.

$$(10) \quad p_{t,4} = \text{CCPR} \cdot p_{t,3}$$

To derive the expression for the total temperature at combustion chamber exit $T_{t,4}$, the energy balance in the combustion chamber is written [16]:

$$(11) \quad \dot{m}_a c_{p,a} T_{t,3} + \dot{m}_f (h_f + H_f \eta_{cc}) = \dot{m}_g c_{p,g} T_{t,4}$$

with $c_{p,a}$ and $c_{p,g}$ respectively the specific heat capacity at constant pressure of the air and the fuel-air gas, \dot{m}_a , \dot{m}_g and \dot{m}_f respectively the mass flow rate of the air, the gas and the fuel, h_f the enthalpy of the fuel entering the combustion chamber, H_f the heating value of the fuel, and η_{cc} the combustion efficiency.

For simplification, the fuel enthalpy h_f is neglected and the following assumption for the mass flow rate of the gas is made $\dot{m}_g = \dot{m}_a + \dot{m}_f$. To reduce the approximation error on the specific heat capacities in the combustion chamber, the mean of their value $\bar{c}_p = (c_{p,a} + c_{p,g})/2$ is considered. An expression for $T_{t,4}$ is subsequently obtained in Eq. 12:

$$(12) \quad T_{t,4} = \frac{\dot{m}_a}{\dot{m}_a + \dot{m}_f} T_{t,3} + \frac{\dot{m}_f H_f \eta_{cc}}{(\dot{m}_a + \dot{m}_f) \bar{c}_p}$$

Turbine 4-5

Similarly to the compressor, the gas expansion in the turbine is subject to losses. The total pressure ratio at turbine exit $p_{t,5}$ can be determined from the turbine total pressure ratio $\Pi_{t,T}$ as in Eq. 13.

$$(13) \quad p_{t,5} = \Pi_{t,T} \cdot p_{t,4}$$

The definition of the turbine isentropic efficiency η_T slightly differs from the compressor isentropic efficiency η_C , as shown in Eq. 14.

$$(14) \quad \eta_T = \frac{T_{t,5} - T_{t,4}}{T_{t,5,is} - T_{t,4}}$$

The resulting expression for the turbine exit temperature is then presented in Eq. 15:

$$(15) \quad T_{t,5} = T_{t,4} \left(1 + \eta_T \left(\Pi_{t,T}^{\frac{\kappa_g - 1}{\kappa_g}} - 1 \right) \right)$$

with κ_g the ratio of specific heat capacities of the gas. Analogously to the compressor, the values for η_T and $\Pi_{t,T}$ are available from component maps.

Nozzle 5-8

The total temperature at nozzle exit $p_{t,8}$ is derived from the nozzle total pressure ratio NPR and a constant value is assumed. As in the inlet, the gas flow is assumed fast enough to be considered adiabatic, additionally, the nozzle is assumed to be adapted to the ambient static pressure p_0 . Hence, the following set of relations in Eq. 16 holds:

$$(16) \quad \begin{aligned} p_{t,8} &= \text{NPR} \cdot p_{t,5} \\ T_{t,8} &= T_{t,5} \\ p_8 &= p_0 \end{aligned}$$

with $T_{t,8}$ the total temperature at nozzle exit, also known as the Exit Gas Temperature (EGT).

The net thrust of the engine F_N , which is the gross thrust minus the drag resulting from the momentum of the incoming air, can be further calculated using the thrust equation in Eq. 17

$$(17) \quad F_N = \dot{m}_g V_8 - \dot{m}_a V_0 + (p_8 - p_0) A_8$$

with V_8 the gas velocity at nozzle exit, and A_8 the nozzle exit area.

With the hypothesis of an adapted nozzle, i.e. $p_8 = p_0$, Eq. 17 can be further simplified, and the resulting expression for the net thrust F_N is described in Eq. 18

$$(18) \quad F_N = \dot{m}_g V_8 - \dot{m}_a V_0$$

The exit gas velocity V_8 is calculated from the Mach number at nozzle exit $M_{a,8}$. The expression for $M_{a,8}$ can be derived from the relation between the total pressure and the static pressure at nozzle exit. This relation has been previously used in Eq. 4

for the calculation of the ambient total pressure $p_{t,0}$. By isolating the Mach number, the expression for $M_{a,8}$ in Eq. 19 is obtained.

$$(19) \quad M_{a,8} = \sqrt{\frac{2}{\kappa_g - 1} \left(\left(\frac{p_{t,8}}{p_8} \right)^{\frac{\kappa_g - 1}{\kappa_g}} - 1 \right)} = \frac{V_8}{\sqrt{\kappa_g R_g T_8}}$$

with R_g the specific gas constant for the exit gas and T_8 the static pressure at nozzle exit. Finally, the expression of T_8 results from the isentropic relation with the previous assumption of an isentropic flow through the nozzle, as shown in Eq. 20.

$$(20) \quad T_8 = T_{t,8} \left(\frac{p_{t,8}}{p_8} \right)^{\frac{1 - \kappa_g}{\kappa_g}}$$

Shaft dynamics

The shaft is connected to the compressor and the turbine and the power chain is the following: the gas flow at combustion chamber exit rotates the axial turbine which in turn drives the compressor through the shaft. To model the dynamics of this process, the power balance in the shaft is written in Eq. 21.

$$(21) \quad P_C + P_S + \eta_m P_T = 0$$

with P_C , P_S and P_T respectively the power available at the compressor, shaft and turbine, η_m the mechanical efficiency of the shaft which accounts for mechanical losses in the transmission. Given that, the Newton's second law motion for moments can be written to express the shaft rotational speed n in Revolutions Per Minute (RPM) as in Eq. 22 [16, 4]:

$$(22) \quad \dot{n} = \frac{dn}{dt} = \frac{-(\eta_m P_T + P_C)}{J \left(\frac{\pi}{30} \right)^2 \cdot n}$$

with J the moment of inertia of the shaft around its rotation axis. Note that, $P_T < 0$ as the turbine outputs power and $P_C > 0$, as the compressor receives power from turbine through the shaft. The expressions for P_T and P_C result from the difference between the total enthalpies at exit and entry of the considered component, and they are detailed in Eq. 23:

$$(23) \quad \begin{aligned} P_C &= \dot{m}_a c_{p,a} (T_{t,3} - T_{t,2}) \\ P_T &= \dot{m}_g c_{p,g} (T_{t,5} - T_{t,4}) \end{aligned}$$

All assumed values for the different gas properties and assumptions on pressure ratios and efficiencies can be found in TAB. 2.

2.4. State space representation

The main governing equations of the turbojet engine have been defined, and it can be observed that the first time derivative of the shaft speed \dot{n} intervenes in the equations as the only higher order term. As a result, the system can be modelled using the state space representation enounced in Eq. 2. The inputs of the system, in accordance with the governing equations, are the fuel mass flow rate \dot{m}_f , and the ambient conditions p_0 , T_0 and V_0 . Having identified the different states

TAB. 2. Assumed values for gas properties and model constants

Symbol	Value	Unit	Symbol	Value	Unit
H_f	43.294	MJ kg ⁻¹	κ_a	1.4	[-]
J	$\frac{1}{2} * 0.2 * 0.025^2$	kg m ²	κ_g	1.33	[-]
CCPR	0.96	[-]	$c_{p,a}$	1006	J kg ⁻¹ K ⁻¹
NPR	0.99	[-]	$c_{p,g}$	1160	J kg ⁻¹ K ⁻¹
IPR	0.98	[-]	$c_{v,g}$	872	J kg ⁻¹ K ⁻¹
R_a	287	J kg ⁻¹ K ⁻¹	η_m	0.99	[-]
R_g	288	J kg ⁻¹ K ⁻¹	η_{CC}	0.95	[-]

and inputs, the following definition in Eq. 24 of vectors of the state space representation in Eq. 2 is adopted.

$$(24) \quad \begin{aligned} \mathbf{X} &= [n]^T & \dot{\mathbf{X}} &= [\dot{n}]^T \\ \mathbf{U} &= [\dot{m}_f]^T & \mathbf{V} &= [p_0, T_0, V_0]^T \\ \mathbf{Y} &= [n, F_N, T_{t,8}]^T \end{aligned}$$

The observed variables in the observation vector \mathbf{Y} are chosen by taking into consideration the available measurement data.

2.5. Component map scaling

The pressure ratio and efficiency of the compressor and turbine have a more complex behaviour, which can be hardly described by simple equations. One of the most well-known tools for assessing the transient behaviour of the compressor and turbine are performance maps. Performance maps are, traditionally, empirical diagrams which map the component pressure ratio and efficiency to the component rotational speed, air mass flow, total pressure and total temperature [16, 6]. The relations between the component map variables are shown in Eq. 25.

$$(25) \quad \begin{aligned} \Pi_{t,C}, \eta_C &= \mathcal{F}(n, \dot{m}_a, p_{t,2}, T_{t,2}) \\ \Pi_{t,T}, \eta_T &= \mathcal{G}(n, \dot{m}_g, p_{t,4}, T_{t,4}) \end{aligned}$$

with \mathcal{F} and \mathcal{G} multivariate unknown functions. When dealing with performance maps, it is more common to introduce the corrected rotational speed $n_{corr,i}$ and corrected air mass flow $\dot{m}_{corr,i}$ with i the corresponding component. The definition of the corrected shaft speed and the corrected mass flow rate result from the expression of their respective non-dimensional form, also called reduced form. The expressions for the reduced mass flow $\dot{m}_{red,i}$ and reduced shaft speed $\dot{m}_{red,i}$, as well as their respective corrected form are given in Eq. 26 for the compressor and in Eq. 27 for the turbine [16, 5].

$$(26) \quad \begin{aligned} n_{red,C} &= \frac{n}{\sqrt{T_{t,2}}} & n_{corr,C} &= \frac{n}{\sqrt{T_{t,2}/T_{isa,MSL}}} \\ \dot{m}_{red,C} &= \frac{\dot{m}_a \sqrt{T_{t,2}}}{p_{t,2}} & \dot{m}_{corr,C} &= \frac{\dot{m}_a \sqrt{T_{t,2}/T_{isa,MSL}}}{p_{t,2}/p_{isa,MSL}} \end{aligned}$$

$$(27) \quad \begin{aligned} n_{red,T} &= \frac{n}{\sqrt{T_{t,4}}} & n_{corr,T} &= \frac{n}{\sqrt{T_{t,4}/T_{isa,MSL}}} \\ \dot{m}_{red,T} &= \frac{\dot{m}_g \sqrt{T_{t,4}}}{p_{t,4}} & \dot{m}_{corr,T} &= \frac{\dot{m}_g \sqrt{T_{t,4}/T_{isa,MSL}}}{p_{t,4}/p_{isa,MSL}} \end{aligned}$$

with $T_{isa,MSL} = 288$ K and $p_{isa,MSL} = 101325$ Pa respectively the temperature and pressure at Mean Sea Level (MSL) according to the International Standard Atmosphere (ISA) model [18]. Additionally, the corrected shaft speed $n_{corr,i}$ is further normalized by the corrected shaft speed at the design operating point $(n_{corr,i})_{design}$, as in Eq. 28, to maintain consistency with different component maps using different design shaft speed.

$$(28) \quad n_{corr,norm,i} = \frac{n_{corr,i}}{(n_{corr,i})_{design}}$$

Finally, the most common representation for a component performance map, given in Eq. 29, can be defined using the previously stated definitions.

$$(29) \quad \begin{aligned} \Pi_{t,C}, \eta_C &= \mathcal{F}(n_{corr,norm,C}, \dot{m}_{corr,C}) \\ \Pi_{t,T}, \eta_T &= \mathcal{G}(n_{corr,norm,T}, \dot{m}_{corr,T}) \end{aligned}$$

As stated previously, component maps are hardly available as such, since they are the product of extensive and expensive testing. They are often not disclosed to the end user for proprietary reasons. Hence, a common method to model the component maps is to use generic component maps from similar components and use a scaling procedure. This method has been first proposed by Kurzke, and is used in the proprietary gas turbine simulation software *GasTurb* [6, 5, 7]. The approach to obtain target component maps from generic ones is illustrated in FIG. 2.

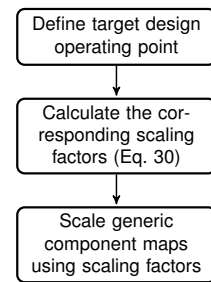


FIG. 2. Component map scaling approach

The scaling factors are empirical formulae to scale the different data-points of the generic component map and they are

detailed in Eq. 30 [6, 5, 7].

$$(30) \quad \begin{aligned} SF_{\dot{m}} &= \frac{\dot{m}_{design,target}}{\dot{m}_{design,generic}} \\ SF_{\Pi_t} &= \frac{\Pi_{t,design,target} - 1}{\Pi_{t,design,generic} - 1} \\ SF_{\eta} &= \frac{\eta_{design,target}}{\eta_{design,generic}} \end{aligned}$$

with $SF_{\dot{m}}$, SF_{Π_t} , SF_{η} respectively the scaling factors for the mass flow rate, the total pressure ratio and the efficiency, $\dot{m}_{design,target}$, $\dot{m}_{design,generic}$ respectively the mass flow rate at the design operating point of the target and generic component map, $\Pi_{t,design,target}$, $\Pi_{t,design,generic}$ respectively the total pressure ratios at the design operating point of the target and generic component map and $\eta_{design,target}$, $\eta_{design,generic}$ respectively the efficiencies at the design operating point of the target and generic component map.

Subsequently, each single data-point of the generic component map is multiplied by the corresponding scaling factors to obtain the scaled performance maps for the target component. For the scaling of the component maps for the P100-RX, generic performance maps are taken from *GasTurb 11* [5], which are stored under a custom format. A script to read generic compressor and turbine performance maps has been written in *Matlab 2019*, likewise, the scaling algorithm has been implemented in the same software. Following this, piecewise cubic surfaces have been fitted to the scaled component maps' data-points in order to use them in simulation. Furthermore, the initial parameters for parameter estimation have been taken from the scaled component maps.

3. EXPERIMENT DESIGN

3.1. DG-800 S Test Bed and Instrumentation

For conducting experiments, an UAV of type *CARF-Models Ltd. DG-800 S* testbed as shown in FIG. 3 is available.



FIG. 3. *CARF-Models Ltd. DG-800 S* test bed with mounted *JetCat P100-RX* turbojet engine.

The testbed is equipped with a range of sensors, including load-cells in the engine mount measuring the force exerted on the airframe by the mounted turbojet engine [19, 20, 21]. The engine *JetCat P100-RX*, is a miniature single spool turbojet engine [17]. It is operated through the ECU which receives throttle commands and monitors the engine state. Furthermore, the ECU is instrumented to gather and transmit sensor values, namely, rotational speed, exhaust gas temperature, fuel flow a.o., during operation with a sampling rate of ca. 20Hz.

In order to determine the thrust force exerted by the engine during flight and ground testing, the sensor readings of the load-cells in the engine mount are converted into force values using a calibration curve. The data for the calibration curve was acquired using a piezo-electric test bench providing force readings in all three dimensions [22] during static thrust experiments. The throttle setting was set to 21 different settings in the range between 0% and 100% in randomized order [23]. By comparing the force values of the test bench and the sensor readings from each of the two sensors at the distinct throttle settings, a calibration curve was derived using the least square method (LSM) [24]. A quadratic function was chosen as the best fit, inspired by similar experiments conducted for the T-FLEX demonstrator [25]. In order to assure the usability of the calibration data for preliminary identification of the transient behaviour, changes from one throttle setting to the next were implemented as a step input.

3.2. DG-800 S Data Characterization

The sample time of the sensor system of the aircraft is about 20 Hz, however, the ECU values do not change in intervals of 20 Hz but more in a region of 5 Hz. This means, multiple identical values are provided in an interval of 20 Hz. Since the area of interest is up to a point of 1.2 Hz, a 5 Hz true sample rate is not ideal, but still well above the Nyquist frequency, which is twice the frequency of interest. Furthermore, the thrust data was taken from the external thrust measurement test stand. This external thrust measurement system provided a sample rate of 100 Hz. During the process of aligning the data using impulses recorded by the on-board systems IMU and the external thrust measurement all data was interpolated to a sample time of approximately 120 Hz. Additionally, as the sensors are inherently subject to clock synchronization issues, a drift of the local timestamps was observed for long testing time spans (ca. 500 ms drift for 8 min testing time). The measured raw thrust data is initially very noisy and a Spencer's 15-point moving average filter was used to smooth the measurements prior to identification [26].

The data set used for system identification is comprised of four multi-sine runs at offsets ranging from 46 % throttle to 85 % throttle, while idle throttle setting is at 33 %. The steps between the offset of the three first multi-sines are also included in the identification data set. The identification data set has a total length of 134 s.

3.3. Input Signal Design

In the interest of reducing the signal injection time, especially later in flight, multi-sine input signals are used. The input signals are designed as described by Morelli [27]. First estimates regarding the frequency span were drawn by applying the *MATLAB* System Identification Toolbox to the step input response data acquired during sensor calibration. After first test runs with the initial multi-sines, the final multi-sine throttle input signals as seen in FIG. 5 (a,c) were designed. In parallel, frequency sweeps were conducted to obtain more detailed test data for evaluating the multi-sine approach. Multiple test runs were conducted with multi-sine, as well as frequency

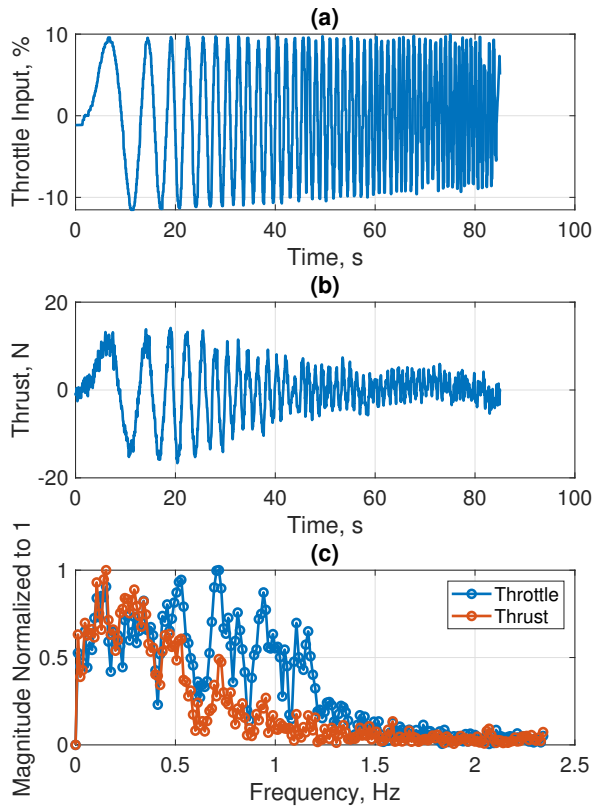


FIG. 4. (a) Frequency sweep input signal, linear trend removed; (b) Frequency sweep answer of the engine, linear trend removed; (c) Fourier analysis of the input and output, the engine was excited up to a frequency of about 1.2 Hz.

sweep, signals varying in amplitude and operating point, i.e. throttle setting. The signals were injected using an *Arduino Nano* driving the PWM throttle command of the ECU.

To present the reaction of the turbine on different input signals, selected, detrended sample data of one of the runs during ground testing is shown in FIG. 4 and FIG. 5. Both figures depict the throttle input in (a) as the system input and the thrust (b) as the system output.

It needs to be noted, that the characteristics between input and output is influenced by the combination of the engine and the ECU. The benchmark model (Eq. 1) has the throttle as input, however, the physical models (based on Eqs. 3 to 30) take the fuel mass flow from the ECU as an input. The result of a Fast Fourier Transformation (FFT) of the input and output signal is shown in FIG. 5 (c) and FIG. 4 (c). Initially the frequency sweep was stopped at about 0.6 Hz, because the engine could not follow the directed throttle input anymore. Irregular and seemingly random behavior occurred. However, lower amplitudes allowed to shift such behaviour up to a frequency of about 1.2 Hz (FIG. 4 (c)). Additionally, the long signal-injection times as used here for the frequency sweep

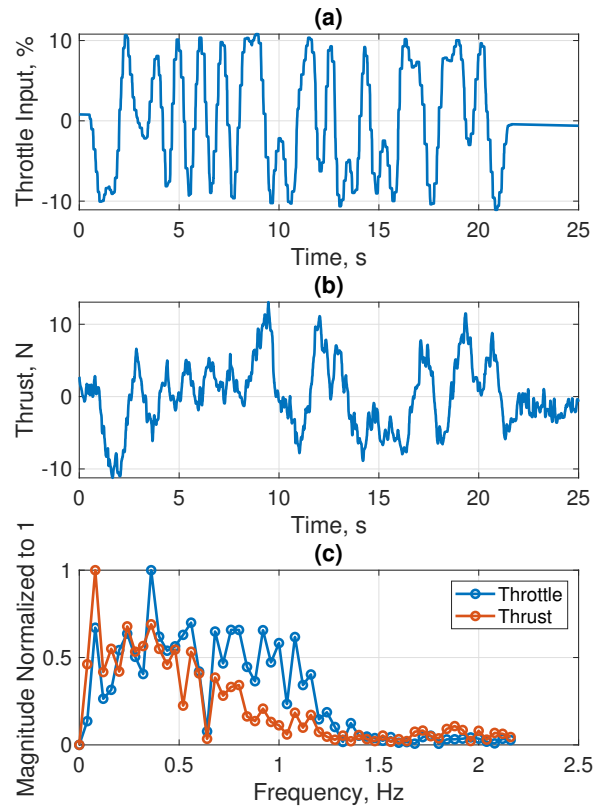


FIG. 5. (a) Multi-sine input signal, linear trend removed; (b) Multi-sine answer of the engine, linear trend removed; (c) Fourier analysis of the input and output, decreasing magnitude of thrust compared to input clearly visible.

are not feasible for in-flight maneuvers. The use of multi-sine inputs mitigates this disadvantage. The answer of the engine thrust to the multi-sine input shows periodic properties (FIG. 5 (b)). Since the multi-sine does not only include eight frequencies as initially, but equally spaced twenty three frequencies ranging from 0.01 Hz up to 1.22 Hz, the different frequencies cannot be distinguished in the rather coarse FFT as shown in FIG. 5 (c)). However, the frequency content is comparable to the one of the frequency sweep FIG. 4 (c)). Comparing the FFT of throttle input to the thrust shows, that the corner frequency is at about 0.4 Hz. This result deviates from the results considering initial estimates based upon step inputs expecting the corner frequency to be at about 1 Hz. Nevertheless, the step-input based estimates were a suitable starting point to position the frequency range included into the multi-sine. The multi-sine input was subsequently adapted from the initial guess based on the information from initial frequency sweeps.

Calculated Bode magnitude plots of the system based on FFT, comparing frequency-sweeps and multi-sines are shown in FIG. 6. Similar results for both methods can be observed.

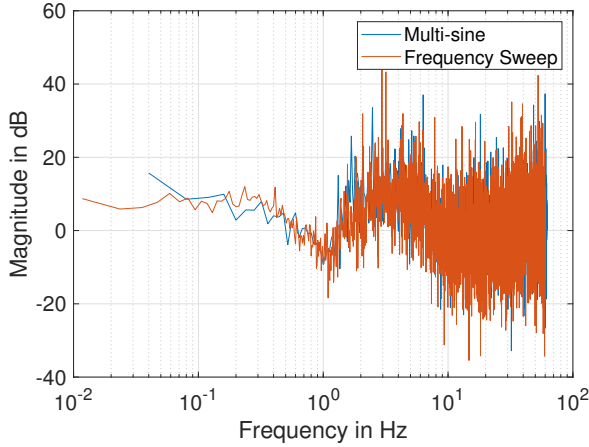


FIG. 6. Bode plot magnitude comparison frequency sweep and multi-sines.

4. SYSTEM IDENTIFICATION

For the system identification of the propulsion system, initially an approach in the frequency-domain was chosen since it has some advantages compared to the time-domain methods, such as reduced dimensionality, noise rejection, accurate model uncertainty characterisation, as well as simple and effective approaches for data filtering [28]. At this time, thrust data was not available, only shaft-speed data, which further simplified the initial guesses. Thus, during closer analysis of the system, the limitation of the frequency domain to linear systems did prove to be insufficient, since the linear models identified were only valid for small operational ranges around the thrust settings at which identification data was collected. Model stitching could have been a solution, however, the choice of formulating a global model as described in the following section was made.

4.1. Methods

The program used for system identification is FALCON.m, an optimal control and parameter estimation toolbox, developed at the Institute of Flight System Dynamics at TUM [13]. The toolbox is implemented in *MATLAB* and provides an efficient interface for integration of new models. The toolbox is computationally faster than most of the competition, since the derivatives required for the numerical optimization are computed analytically via the *Matlab Symbolic Math Toolbox*. The model and the cost function (including the relevant derivative computations) are coded in C and evaluated via the Matlab .mex interface. This improves the computational speed significantly, compared to the evaluation of the same functions in the Matlab environment.

The initial parameter values for identification were computed from scaled component maps. As a cost function the Maximum Likelihood was chosen to implement an output error method, as in Eq. 31.

$$(31) \quad J(\Theta) = \frac{1}{2} \sum_{i=1}^N [z(i) - y(i)]^T R^{-1} [z(i) - y(i)] + \frac{N}{2} \ln(|R|)$$

where Θ is the parameter vector, N the number of discrete data points over the runtime, z are the measurements and y is the vector of the model outputs. The matrix R is the noise covariance matrix. The (diagonal) elements of this matrix are also determined during the optimization via a two step relaxation strategy which is also described in [29].

The Levenberg-Marquardt optimization algorithm was applied to minimize the above cost function, since it proves to be more robust than the Gauss-Newton Algorithm [30].

The system identification process is a compromise between reducing the remaining parameter uncertainties, while trying to get realistic component map predictions, maintaining an acceptable model fit to the experiment data. Relative standard deviations (RSD), which are relative to the parameter values, and the correlation matrix has been used to numerically assess the remaining uncertainty in the estimated parameter values. The a priori values for the parameters were varied and adapted based on component map predictions derived from *GasTurb*, as well as qualitative analysis of aforementioned metrics and fits.

4.1.1. Physical base Model

The first physics-based model is based on the state space representation of the section 2.4. The component maps are approximated using quadratic functions and modelled as a function of the shaft speed n only. This choice results mainly from the fact that available measurements are limited (thrust, EGT and shaft speed) and that the number of parameters is to be kept low for meaningful parameter identification. The approximation function models are presented in Eqs. 32

$$(32) \quad \begin{aligned} \Pi_{t,C}(n) &= CPR_0 + CPR_1 n + CPR_2 n^2 \\ \Pi_{t,T}(n) &= TPR_0 + TPR_1 n + TPR_2 n^2 \\ \eta_C(n) &= \eta_{c0} + \eta_{c1} n + \eta_{c2} n^2 \\ \eta_T(n) &= \eta_{t0} + \eta_{t1} n + \eta_{t2} n^2 \end{aligned}$$

with CPR_i , TPR_i , η_{ci} , η_{ti} the coefficients to be identified in the approximation functions. Furthermore, simple mass flow dynamics were added in order to shift the values of the estimated parameters in physically more plausible areas. The mass flow approximation model is presented in Eq. 33:

$$(33) \quad \dot{m}_3(n) = \dot{m}_{3,0} + \dot{m}_{3,1} n$$

To compensate for the convection dynamics of the temperature sensor for the EGT $T_{t,8}$, a first order LTI behaviour was assumed. The dynamics were modelled according to Eq. 34.

$$(34) \quad \dot{T}_{t,8,m} = \frac{1}{\tau} (KT_{t,8,true} - T_{t,8,m})$$

with $T_{t,8,m}$ the actual measured temperature and $T_{t,8,true}$ the true temperature resulting from model calculations. An estimation of the gain K was attempted, in order to retrieve the

recovery factor of the thermal sensor, which is the difference between true total temperature and measured total temperature due to non isentropic accumulation. This attempt resulted in a negligible gain close to 1. The gain K is thus assumed to be 1, as no measurable bias for the steady-state temperature value is introduced by the sensor. The time constant τ was estimated to be 3.029 s, with a RSD of under 1 % and was set as fixed for further parameter estimation.

In order to include this behaviour, another state for the measured temperature $T_{t,s,m}$ was introduced in the state space representation from Eq. 2. Accordingly, the new considered vectors are stated in Eq. 35:

$$(35) \quad \begin{aligned} \mathbf{X} &= [n, T_{t,s,m}]^T & \dot{\mathbf{X}} &= [\dot{n}, \dot{T}_{t,s,m}]^T \\ \mathbf{U} &= [\dot{m}_f]^T & \mathbf{V} &= [p_0, T_0, V_0]^T \\ \mathbf{Y} &= [n, F_N, T_{t,s,m}]^T \end{aligned}$$

4.1.2. Simplified Physical Model with Thrust Mapping

This model is a reduction of the model described in 4.1.1. Hereby, an attempt was made to map the thrust directly from the shaft dynamics described in chapter 2.3.1 as a simple polynomial function. For that, a certain number of step inputs experiments were conducted and the steady state thrust was measured for a given range of shaft speed values. Subsequently, a fourth order polynomial function as in Eq. 36 was then identified on a scatter plot of the measured thrust over the shaft speed n .

$$(36) \quad F_N(n) = F_{n0} + F_{n1} \frac{n}{10^4} + F_{n2} \left(\frac{n}{10^4}\right)^2 + F_{n3} \left(\frac{n}{10^4}\right)^3 + F_{n4} \left(\frac{n}{10^4}\right)^4$$

The shaft speed was divided by 10^4 , in order to avoid values close to the numerical zero for the parameters F_{ni} . The motivation behind this approach was to use a nondynamic relation between shaft speed and thrust in order to simplify the base model.

In this approach only a mapping of the thrust from the shaft speed is considered, hence an observation of the EGT is not needed. The resulting vectors for the state space representation are presented in Eq. 37:

$$(37) \quad \begin{aligned} \mathbf{X} &= [n]^T & \dot{\mathbf{X}} &= [\dot{n}]^T \\ \mathbf{U} &= [\dot{m}_f]^T & \mathbf{V} &= [p_0, T_0, V_0]^T \\ \mathbf{Y} &= [n, F_N]^T \end{aligned}$$

4.2. Results

In this section, the results of parameter identification on the previously derived models are presented. The identified parameters were removed based on analysis of the correlation and relative standard deviation values. This means, that parameter values that do not appear in TABs. 4 and 5 are set to zero in order to reduce linear correlations and standard deviations.

4.2.1. Benchmark Model

The benchmark model, which was presented in section 2.1 has been identified from the measurements of throttle and thrust from the turbine. For that, initial parameter values were directly taken from the result of the work of L'Erario et al.. Subsequently, parameter identification using multi-sine inputs, described in section 3.2, is performed and the resulting estimated parameters are presented in TAB. 3.

TAB. 3. Parameters values with relative standard deviation (RSD) of the benchmark model.

Parameter	Value	RSD in %
B_{UU}	2.33×10^{-2}	± 36.48
B_D	-1.76×10^{-2}	± 20.71
B_T	3.36×10^{-2}	± 33.45
B_U	6.52×10^{-1}	± 17.08
c	-5.71×10^1	± 4.93
K_{TD}	9.81×10^{-2}	± 14.33
K_{DD}	5.28×10^{-2}	± 10.63
K_D	-5.60	± 4.91
K_{TT}	-1.55×10^{-1}	± 3.48
K_T	-1.13	± 29.21

The relative standard deviation (RSD) of the model parameters range from about 3.5 % to 36.48 %, which indicates high to medium confidence on the estimated parameters. Furthermore, the parameter correlation matrix, shown in FIG. 7, was computed to gather information on the linear interdependencies between the parameters. High correlations for

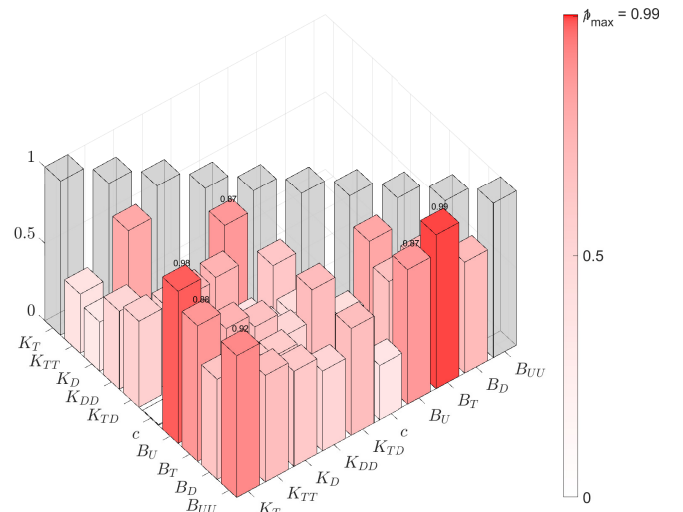


FIG. 7. Correlation matrix of the parameters of the benchmark model.

the parameters $B_U - B_{UU}$ of 0.99, and $B_U - K_T$ of 0.98 can be

observed. All other correlation factors are below the threshold of 0.95, which commonly serves as reference to assume acceptable correlation between parameters in aircraft system identification [26]. However, special attention needs to be directed to values over 0.90.

Observing the model fit on validation data in FIG. 12 the model thrust deviates from the measured thrust within a range of thrust of ca. -8.6 N to 8.8 N , which is a maximum span of 17.4 N . Furthermore, at low thrust levels the relative fit is worse, but the absolute deviation from the measured values stays approximately the same over the course of the validation data. In order to improve the fit, a priori knowledge in form of the physical equations derived in section 2 is used. This also permits to use more measurements than only throttle input and thrust. Intermediate results, such as the shaft speed and the exit gas temperature can also be used as outputs and as such be fitted to measured data (Eq. 2).

4.2.2. Physical model

Parameter values derived by the system identification method described above are shown in TAB. 4. Most RSDs are in a range between 0.94% and 3.17%, only the constant mass flow parameter has a relatively high RSD of 44.72%. Looking at the

TAB. 4. Parameters values with first relative standard deviation (RSD) of the physical model.

Parameter	Value	RSD in %
CPR_0	1.54	± 3.17
CPR_1	9.22×10^{-6}	± 2.66
TPR_0	7.44×10^{-1}	± 1.32
TPR_1	-3.92×10^{-6}	± 1.02
η_{c0}	4.87×10^{-1}	± 1.67
η_{c1}	5.69×10^{-6}	± 1.91
η_{c2}	-3.43×10^{-11}	± 0.94
η_{t0}	4.44×10^{-1}	± 1.33
η_{t1}	-1.43×10^{-6}	± 1.22
$\dot{m}_{3,0}$	-1.14×10^{-3}	± 44.72
$\dot{m}_{3,1}$	6.79×10^{-7}	± 1.78

correlation matrix in FIG. 8 numerous quite high correlation factors can be seen. Two with a value of 0.98, one of 0.97, one of 0.96 and two of 0.95. All other correlation factors are below the threshold of 0.95.

The resulting component map predictions are shown in FIG. 4.2.2. The resulting equations plotted over the shaft speed in FIG. 4.2.2 are all linear, except for η_c . The predictions for $\Pi_{t,C}$, $\Pi_{t,T}$ and η_c are physical feasible and were expected as such. η_T is lower than expected and should increase with increasing RPM. Trying to force η_T to be at least constant resulted in complex values during the estimation. \dot{m}_3 is lower than expected, since the manufacturer states a nominal mass flow for the engine of 0.23 kg s^{-1} (TAB. 1). The model fit to validation data in FIG. 12 shows an offset of ca. $+2.5 \text{ N}$, which is established after about 2 s and maintained throughout the test run. The model thrust deviates from the measured thrust within a range of ca. -4.8 N to 10.5 N , which

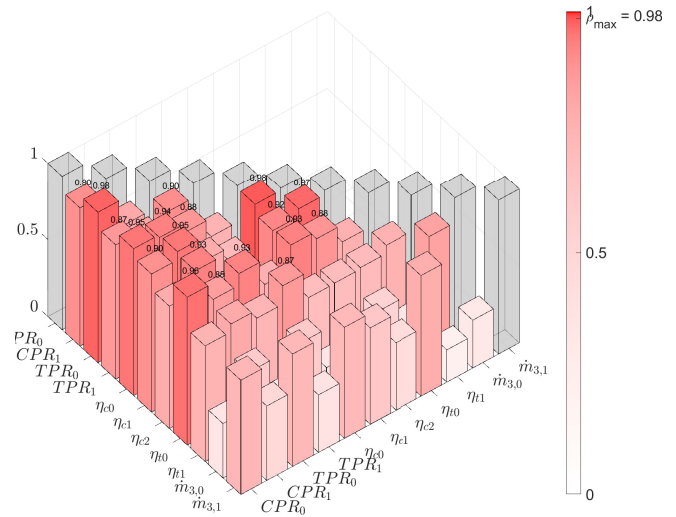


FIG. 8. Correlation matrix of the parameters of the physical model.

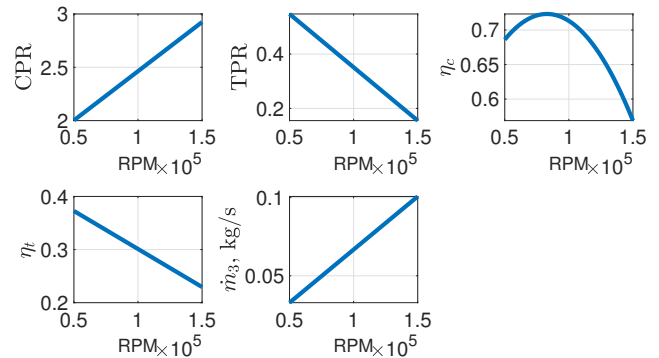


FIG. 9. Component map predictions of the physical model.

is a maximum span of 15.3 N , performing slightly better than the phenomenological model. In low thrust regions, the thrust of the physical model follows the contours of the measured thrust better than the phenomenological model. However, the constant offset mostly yields a higher residual thrust in those areas.

4.2.3. Simplified Physical Model with Thrust Mapping

The resulting parameters of this approach are listed in TAB. 5. Here, it can be observed, that the RSDs of some parameters are very high, even though the same amount of parameters as before were estimated. However, removing more parameters in order to counter such high RSDs resulted in a bad fit of the validation data (FIG. 12). Notable is, that the RSDs of the two mapping parameters F_{n1} and F_{n4} are very low and could thus be determined with high confidence. The correlation matrix in Fig. 10 is filled with high correlation coefficients.

TAB. 5. Parameters values with first relative standard deviation (RSD) of the physical model with direct thrust mapping.

Parameter	Value	RSD in %
CPR_0	1.35	± 4549.93
CPR_1	6.47×10^{-6}	± 12240.54
TPR_0	7.11×10^{-1}	± 25.32
TPR_1	-2.90×10^{-6}	± 8.24
η_{c0}	8.01×10^{-1}	± 15779.4
η_{c1}	4.53×10^{-6}	± 788.12
η_{c2}	-3.86×10^{-11}	± 7530.62
η_{t0}	3.85×10^{-1}	± 49.84
$\dot{m}_{3,1}$	1.46×10^{-6}	± 634.47
F_{n1}	7.88	± 0.31
F_{n4}	1.2×10^1	± 0.11

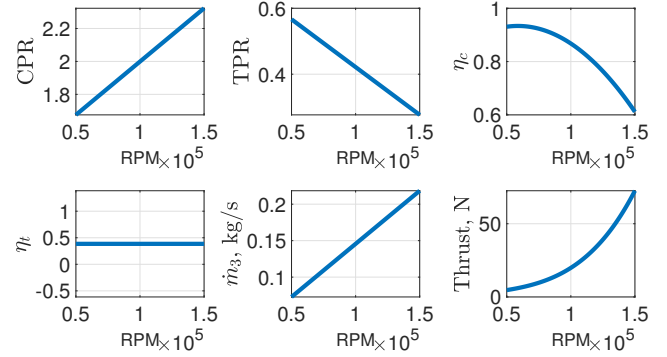


FIG. 11. Component map predictions of the physical model with direct thrust mapping and on the bottom right the mapping of the thrust to the RPM.

Nineteen are above the threshold of 0.9, thereof seven are 1. All other correlation coefficients are very well below 0.5. Most

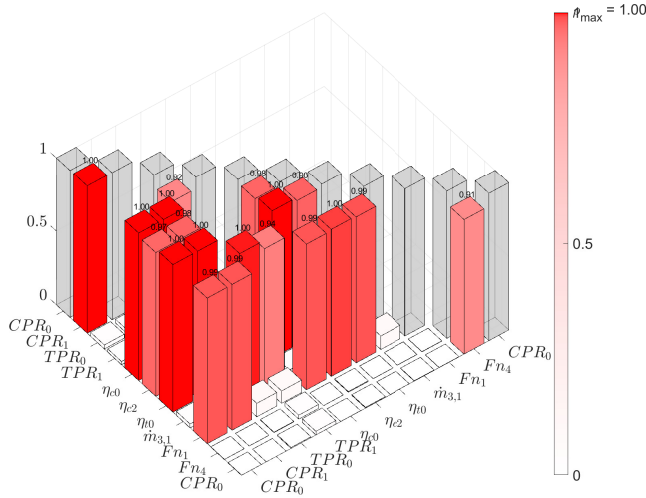


FIG. 10. Correlation matrix of the parameters of the physical model with direct thrust mapping.

of the parameters of the mapping function in Eq. 36 are eliminated due to high correlation coefficients. The remaining parameters F_{n1} and F_{n4} show no linear dependency on any parameters. The component map predictions shown in FIG. 11 are comparable to those of the original physical model. The predictions for $\Pi_{t,C}$ and $\Pi_{t,T}$ are lower. η_C reaches almost one. η_T is lower than expected and approximated as constant. \dot{m}_3 is closer to the expected value, as the expected nominal air mass flow rate of 0.23 kg s^{-1} is almost reached. However needs to be stated, that the optimisation of the cost function did not converge for this model. The number of iterations were chosen, so that the component map predictions do not exceed physical possible values. The first value to get unphysical was the efficiency of the compressor η_C , which ex-

ceeded one. On the bottom right of FIG. 11 eq. 36 is plotted, only depended on the RPM and the two parameters F_{n1} and F_{n4} . The model fit to validation data in FIG. 12 is almost indistinguishable from the fit of the previous physical model, also having a constant offset.

To further investigate the offset seen in both models, an exemplary fit on multi-sine validation data for the shaft dynamics can be seen in FIG. 13. The observed offset is only present on the validation data, and no offset was noticeable on the identification data. After removing the offset, the model response for the shaft speed is close to measured values as can be seen in FIG. 13.

5. DISCUSSION

Multi-sines proved to be an efficient tool, not only for multiple input/multiple output systems, as demonstrated in [28], but also for single input single output systems in order to cut down test time. They are comparably simple to design and thus adaptable to the current use-case. The benchmark phenomenological model provided a good fit without modification, with inaccuracies in lower thrust regions below 20 N . However, all models lose accuracy when modelling the jet engine behaviour at low thrust settings. This could be because of changing dynamics in low thrust regions due to lower involved speeds. Furthermore, additional parameters of the benchmark phenomenological model could be eliminated when analyzing the RSDs and correlation matrix, however the resulting fit loses in accuracy. Moreover, a modelling from throttle input to shaft speed includes the dynamics of the fuel pump and potential controller in the ECU, in contrast to the physical models.

The physical base model (see section 4.1.1) shows potential, since most RSDs are already very low and most component map predictions are physically feasible. The correlation matrix in FIG. 8 is populated partly by very high values up to 0.98. However in order to keep most of the component map predictions realistic further parameter reduction is difficult. Here, future work on the system dynamics could probably provide a better model. The model fit is slightly better compared to the

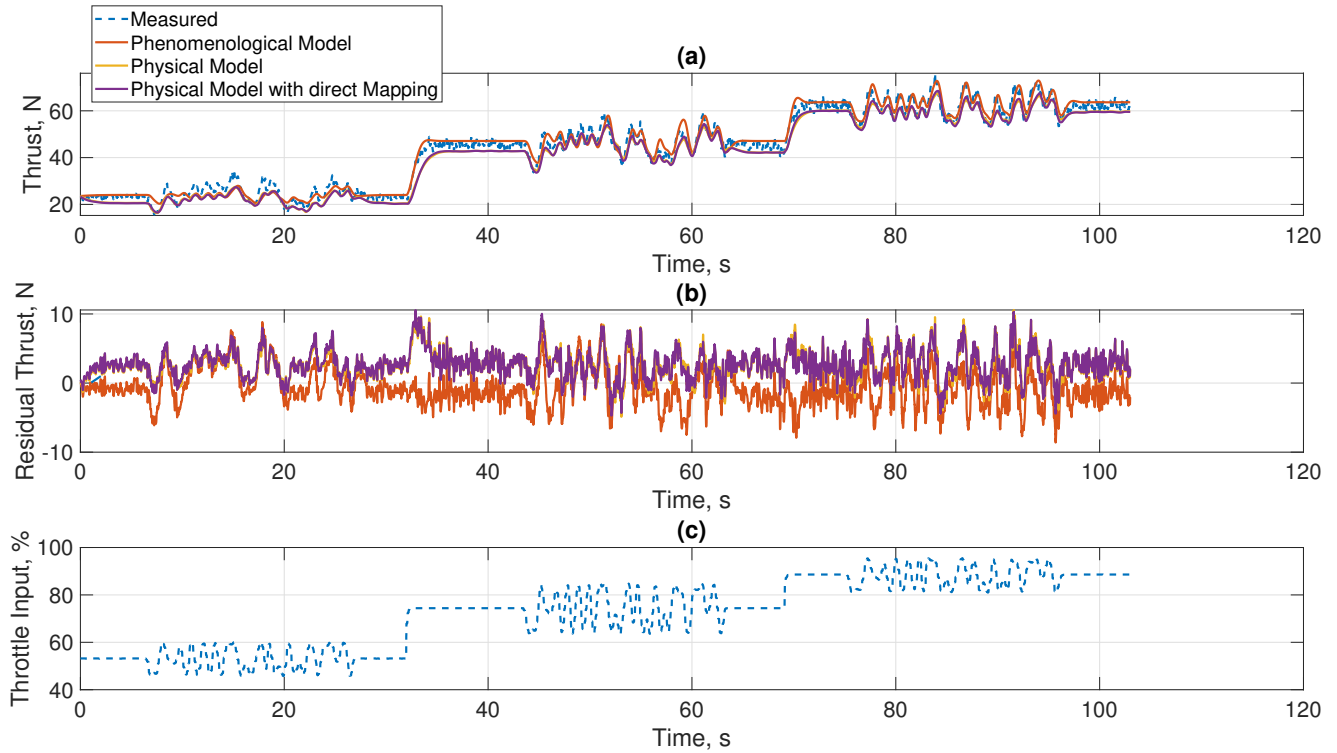


FIG. 12. Comparison of the outputs of the different models on validation data not used for identification; (a) thrust fit comparison, the response of the physical model and the physical model with mapping are nearly identical; (b) residual comparison; (c) throttle input, 33 % equals idle speed. Thin lines kept for better distinguishability between the models

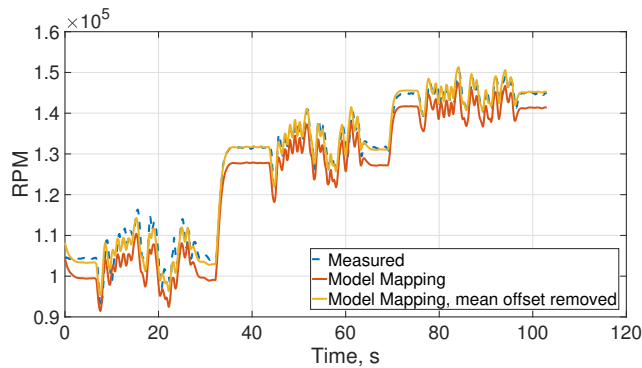


FIG. 13. Fit of the shaft speed of the physical model with mapping on validation data. With offset and mean offset removed.

phenomenological model in FIG. 12, especially when compensating for the offset of the physical mode. As can be seen in FIG. 13 this offset is not only existent for the thrust (FIG. 12) when applying the model to validation data, but also in the shaft dynamics. This observation yields the notion, that the offset error should be originating in the shaft dynamics and is not a problem with faulty thrust measurement.

The simplified physical model with thrust mapping yields the same fit quality as the physical base model, while including simpler dynamics. However, most RSDs, correlation coefficients and component map predictions look a lot worse, which does not yield much confidence in the estimated parameters, as well as in the model structure. (FIG. 5, FIG. 10, FIG. 11). A reason could be the same amount of identified parameters for the model with mapping as for the physical base model in contrast to less measured information available due to the unused measurement of the EGT. Regardless, the RSDs and correlation coefficients of the mapping parameters F_{n1} and F_{n4} are very low, which provides great confidence in those. Overall, this approach demonstrates that the mapping from shaft speed to thrust can yield sufficient results to reduce model complexity, given that an adequate model fit for the shaft speed is available.

6. OUTLOOK

The approaches presented here prove that the feasibility of system identification based on physics-based nonlinear models is sounded. The presented models have their advantages and disadvantages, and future work is to be carried out to perfect the model structure, together with a consideration of neglected dynamics, such as for instance the dynamics in the combustion chamber. Additional work on the approximation of component map functions can be conducted along with more reliable initial parameters in order to find better optimums. With more measurements of the state of the gas flow (pressure, temperature) at the different stations of the engine, more information can be introduced, which could enable this approach to yield better results, in particular for component map predictions. This approach is exemplified in the following sections.

6.1. Alternative state space representation

In this section, an alternative modelling of the system is considered which introduces 2 additional states in the state vector \mathbf{X} : the total pressure and total temperature at combustion chamber exit $p_{t,4}$ and $T_{t,4}$. The new expression for the state \mathbf{X} becomes:

$$(38) \quad \mathbf{X} = [n, p_{t,4}, T_{t,4}]^T$$

This modeling approach has been considered by Kulikov Thompson [16] and Beneda et al. [10] for the derivation of a linear state space model from the linearization of the equations of the nonlinear model. The state transition differential equations are given in Eqs. 39, 40, 41 :

$$(39) \quad \frac{dn}{dt} = \frac{-(\eta_m P_T + P_C)}{J(\frac{\pi}{30})^2 \cdot n}$$

$$(40) \quad \dot{p}_{t,4} = \frac{p_{t,4}}{T_{t,4}} \dot{T}_{t,4} + \frac{R_g T_{t,4}}{V_{CC}} (\dot{m}_3 + \dot{m}_f - \dot{m}_4)$$

$$(41) \quad \dot{T}_{t,4} = \frac{1}{c_{v,g} m_{CC}} [(\dot{m}_3 h_{t,3} + \dot{m}_f H_f \eta_{CC} - \dot{m}_4 h_{t,4}) - c_{v,g} T_{t,4} (\dot{m}_3 + \dot{m}_f - \dot{m}_4)]$$

with V_{CC} the volume of the combustion chamber, m_{CC} the fluid mass in the combustion chamber, $c_{v,g}$ the isobaric specific heat capacity of the gas, $h_{t,3}$ and $h_{t,4}$ respectively the total/stagnation enthalpies at combustion chamber inlet and exit.

The governing equations are similar to the previously detailed equations with the difference that in this representation, $p_{t,4}$ and $T_{t,4}$ result from the solution to the ordinary differential equations for state transition (Eqs. 40, 41). Hence, the new governing equations are detailed in the following FIG. 14:

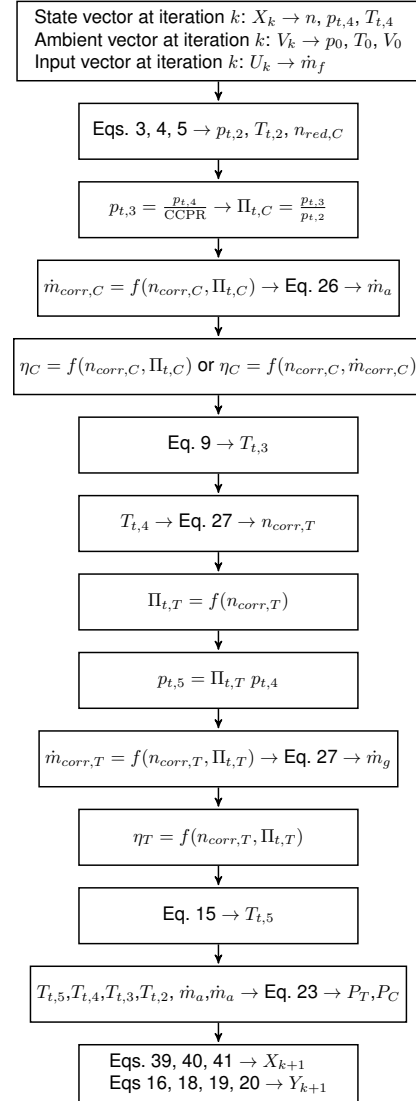


FIG. 14. Approach for an alternative nonlinear modelling of the turbojet engine

The unknown functions f in FIG. 14 can be approximated using polynomial functions and can be further estimated using parameter identification. In this work, the coefficients of the polynomial approximations are used as parameters in the parameter vector Θ . Initial parameters for these functions are taken from the scaled component maps. This nonlinear model poses a certain number of disadvantages: the time derivative of the state $p_{t,4}$ depends on the derivative of state $T_{t,4}$, the required simulation time step for parameter identification needs to be set extremely low. This complicates parameter identification and all identification attempts were unsuccessful, although simulation with initial parameters for the component maps were already close to the measured data, as shown in FIG. 15, exemplifying the inherent potential of this approach.

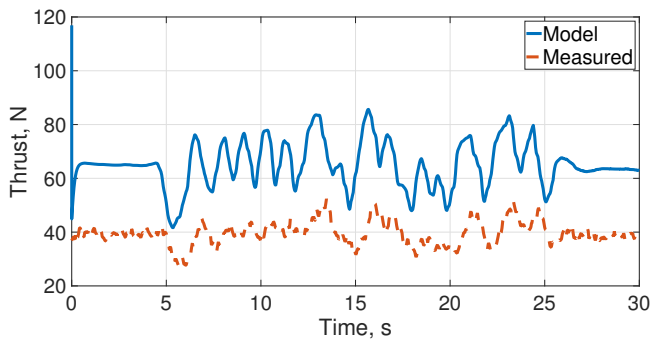


FIG. 15. Simulation run of the alternative state space model with multi-sine input using the initial parameters derived from scaled component maps.

In order to perform identification on the alternative state space representation, the system identification tool *Falcon.m* can be further extended in order to deal with inter-dependencies between the state derivatives of $p_{t,4}$ and $T_{t,4}$. Introducing delays on the state derivatives is one way to tackle this problem. Finally, more measurements from flight tests are needed to complement the system identification approach.

7. REFERENCES

- [1] Philipp Stahl, Franz-Michael Sendner, Andreas Hermanutz, Christian Rößler, and Mirko Hornung. Mission and Aircraft Design of FLEXOP Unmanned Flying Demonstrator to Test Flutter Suppression within Visual Line of Sight. In *17th AIAA Aviation Technology, Integration, and Operations Conference 2017*, page 11, Red Hook, NY, 2017. Curran Associates Inc. ISBN 978-1-62410-508-1. doi: 10.2514/6.2017-3766.
- [2] Franz-Michael Sendner. *Evaluierung und Auswahl von geeigneten Antriebslösungen für ein unbemanntes Forschungsfluggerät*. Master's Thesis, Technical University of Munich, Munich, 2016.
- [3] Vinzenz Brandtner. *Erweiterung eines Triebwerksmodells zur Berücksichtigung von Einlaufstörungen mittels MATLAB / Simulink*. Master's Thesis, Technical University of Munich, Munich, 2019.
- [4] Christiaan van Ommeren. *Dynamische Simulation einer Modellgasturbine mit MATLAB/Simulink*. Semester's Thesis, Technical University of Munich, Munich, 2015.
- [5] Joachim Kurzke. Design and off-design performance of gas turbines. *Gasturb 11 Manual*, 2007.
- [6] Joachim Kurzke and Claus Riegler. A New Compressor Map Scaling Procedure for Preliminary Conceptual Design of Gas Turbines. volume Volume 1: Aircraft Engine; Marine; Turbomachinery; Microturbines and Small Turbomachinery of *Turbo Expo: Power for Land, Sea, and Air*, 05 2000. doi: 10.1115/2000-GT-0006. URL <https://doi.org/10.1115/2000-GT-0006>. V001T01A006.
- [7] C. Kong, J. Ki, and M. Kang. A new scaling method for component maps of gas turbine using system identification. *Journal of Engineering for Gas Turbines and Power*, 125(4):979–985, 2003. doi: 10.1115/1.1610014.
- [8] Nicholas D. Grannan, Michael J. McClearn, Paul J. Litke, John Hoke, and Frederick Schauer. Trends in jetcat microturbojet-compressor efficiency. *55th AIAA Aerospace Sciences Meeting*, 2017. doi: 10.2514/6.2017-0552.
- [9] Henrique Gazzetta Junior, Cleverson Bringhenti, João Roberto Barbosa, and Jesuino Takachi Tomita. Real-time gas turbine model for performance simulations. *Journal of Aerospace Technology and Management*, 9:346–356, 2017. ISSN 21759146. doi: 10.5028/jatm.v9i3.693.
- [10] Károly Beneda, Rudolf Andoga, and Ladislav Főző. Linear mathematical model of single-spool micro turbojet engine with fixed exhaust nozzle. In *2018 IEEE 16th World Symposium on Applied Machine Intelligence and Informatics (SAMII)*, pages 000017–000022. IEEE, 2018.
- [11] Károly Beneda and Ladislav Főző. Identification of small scale turbojet engine with variable exhaust nozzle. In *2017 IEEE 15th International Symposium on Applied Machine Intelligence and Informatics (SAMII)*, pages 000073–000078. IEEE, 2017.
- [12] Sinan Ekinci, Ali Türker Kutay, Oğuz Uzol, and Melih Yiğittürk. System identification and controller development for a small turbojet engine. 6. ANKARA INTERNATIONAL AEROSPACE CONFERENCE, (14-16 September 2011), 2011. URL <https://hdl.handle.net/11511/78003>.
- [13] Matthias Rieck, Matthias Bittner, Benedikt Grüter, Johannes Diepolder, and Patrick Piprek. *Falcon.m user guide*. URL www.falcon-m.com.
- [14] Eugene Morelli. System Identification Programs for Aircraft (SIDPAC). In *AIAA Atmospheric Flight Mechanics Conference and Exhibit*, Reston, Virginia, 08052002. American Institute of Aeronautics and Astronautics. ISBN 978-1-62410-107-6. doi: 10.2514/6.2002-4704.
- [15] Giuseppe L'Erario, Luca Fiorio, Gabriele Nava, Fabio Bergonti, Hosameldin Awadalla Omer Mohamed, Emilio Benenati, Silvio Traversaro, and Daniele Pucci. Modeling, identification and control of model jet engines for jet powered robotics. *IEEE Robotics and Automation Letters*, 5(2):2070–2077, 2020. doi: 10.1109/LRA.2020.2970572.
- [16] Gennady Kulikov and Haydn Thompson. *Dynamic Modelling of Gas Turbines: Identification, Simulation, Condition Monitoring and Optimal Control*. 01 2004. ISBN 978-1-84996-914-7. doi: 10.1007/978-1-4471-3796-2.
- [17] P100-RX - JetCat. URL https://www.jetcat.de/en/productdetails/produkte/jetcat/produkte/hobby/Engines/p100_rx.
- [18] ISO 2533:1975. Standard atmosphere. Standard, International Organization for Standardization, Geneva, CH, May 1975.
- [19] Edwin-Alejandro Ploetz Simavilla. *Development and implementation of an on-board thrust measurement system for UAV applications*. *Entwicklung und Implemen-*

- tierung eines on-board Schubmesssystems für UAV-Anwendungen. Master's Thesis, Technical University of Munich, Munich, 2020.
- [20] Lars Nagel. *Instrumentation and Flight Testing of a UAV of Type DG-800 S*. Bachelor's Thesis, Technical University of Munich, Munich, 02.11.2020.
 - [21] Luis de Magalhães Ross, Victor. *Instrumentation and Flight Testing of a UAV of type DG-800 S. Instrumentierung und Flugerprobung eines unbemannten Fluggerätes des Typ DG-800 S*. Bachelor's Thesis, Technical University of Munich, Munich, 2020.
 - [22] Lykourgos Bougas and Mirko Hornung. Propulsion system integration and thrust vectoring aspects for scaled jet uavs. *CEAS Aeronautical Journal*, 4(3):327–343, 2013.
 - [23] Sebastian Oberndorfer. *Charakterisierung und Kalibrierung eines Sensorsystems zum Einsatz auf einem UAV des Typs DG-800 S*. Bachelor's Thesis, Technical University of Munich, Munich, 2021.
 - [24] Massimiliano Bonamente. *Statistics and analysis of scientific data*. Springer, New York, NY, 2018. ISBN 9781493982394.
 - [25] Jonas Koch. *Design and Development of a Jet Engine Thrust Measurement System for in-Flight Applications*. Semester Thesis, Technical University of Munich, Munich, 2020.
 - [26] Ravindra V. Jategaonkar. *Flight Vehicle System Identification: A Time-Domain Methodology, Second Edition*. American Institute of Aeronautics and Astronautics, Inc., 1 2015. ISBN 978-1-62410-278-3. doi: 10.2514/4.102790. URL <http://arc.aiaa.org/doi/book/10.2514/4.102790>.
 - [27] Eugene A. Morelli. Flight test maneuvers for efficient aerodynamic modeling. *Journal of Aircraft*, 49(6):1857–1867, 2012. ISSN 0021-8669. doi: 10.2514/1.C031699.
 - [28] Eugene A. Morelli and Jared A. Grauer. Practical aspects of frequency-domain approaches for aircraft system identification. *Journal of Aircraft*, 57(2):268–291, 2020. ISSN 0021-8669. doi: 10.2514/1.C035599.
 - [29] V. Klein and Eugene Morelli. *Aircraft System Identification: Theory And Practice*. 08 2006. doi: 10.2514/4.861505.
 - [30] Donald W. Marquardt. An algorithm for least-squares estimation of nonlinear parameters. *Journal of the Society for Industrial and Applied Mathematics*, 11(2):431–441, 1963. doi: 10.1137/0111030. URL <https://doi.org/10.1137/0111030>.